Three-dimensional Overturning Circulation Generated by Topography in the Southern Ocean and Its Implications

Madeleine K. Youngs [1], **Glenn R. Flierl** [2]

[1]NYU, Courant Institute of Mathematical Sciences
[2]MIT, Department of Earth, Atmospheric, and Planetary Sciences

Key Points:

- This study investigates how the topography of the Southern Ocean leads to three-dimensionality of the overturning in an idealized channel.
- Overturning is composed of three parts: a wind-driven Ekman transport, standing eddies and transient eddies.
- The localization of standing and transient eddy processes weakens the response of the overturning to changes in wind.

Corresponding author: Madeleine K. Youngs, my2368@nyu.edu

Abstract

The Southern Ocean plays a major role in the global air-sea carbon fluxes, with some estimates suggesting it takes up 40% of the total anthropogenic carbon dioxide. Understanding the Southern Ocean overturning transport is particularly important because the overturning transport fluxes tracers between the depth and the surface. Recent work shows that this vertical transport preferentially occurs downstream of bottom topography, but there is further work to understand how this relates to the theory of overturning circulation. This study uses an idealized Southern Ocean-like MITgcm channel and particle tracking in the thickness-weighted circulation to develop a new understanding of the three dimensional-nature of the overturning. This study evaluates the overturning transport by splitting the flow into three main driving forces behind the transport. First, is a wind-driven Ekman transport which is spread out throughout the domain and only leading order in the upper overturning cell, although not entirely zonally-symmetric due to the meandering nature of the flow. The remaining two components are standing eddies and transient eddies both of which are localized near the topography. The existence of the ridge weakens the response of the overturning to changes in wind, especially in the lower cell. The localization of the vertical flow shows the necessity of careful modeling of these specific regions in the Southern Ocean to understand the transport and carbon export.

Plain Language Summary

The Southern Ocean is a key location for the global carbon budget because it is where the deep ocean interfaces with the atmosphere and exchanges long held carbon reserves. This study uses an idealized channel model to see how the surface ocean connects to the deep ocean and find that almost all of this connection is right near the topographic features. The localization due to the undersea ridge reduces the sensitivity of the vertical transport to changes in wind. This points to the importance of sampling and modeling these localized regions carefully in order to capture the local eddy activity.

1 Introduction

The Southern Ocean is responsible for about 30% to 40% of oceanic anthropogenic carbon uptake, an oversized contribution (Gruber et al., 2009; Frölicher et al., 2015). How that carbon budget has varied since the industrial revolution and how the budget will change with climate change are open questions (Le Quéré et al., 2017). Since there is a strong vertical gradient in dissolved inorganic carbon in the near-surface Southern Ocean (Gruber et al., 2009), the vertical transport of water is a major physical process affecting the air-sea carbon fluxes. Thus an understanding of upwelling is necessary to understand the carbon budget.

Traditionally, we call the circulation responsible for the upwelling of tracers the residual overturning circulation. This is called the residual circulation because it is the small remainder of two main competing processes, wind-driven overturning that steepens isopycnals and eddy-driven overturning that acts to relax those isopycnals (Marshall & Speer, 2012). This understanding was developed for an idealized ocean that lacks bottom topography or other zonal asymmetries. Many other aspects of this theory have been shown to be overly simple due to the existence of topography (Youngs et al., 2017, 2019; R. Abernathey et al., 2011). There is still then the open question of how the topography modifies the overturning circulation and changes its response to changes in wind.

Currently there is little understanding of how the residual overturning in the Southern Ocean responds dynamically to changes in wind stress and buoyancy forcings, with most studies considering the steady state overturning and constant forcings (Hallberg

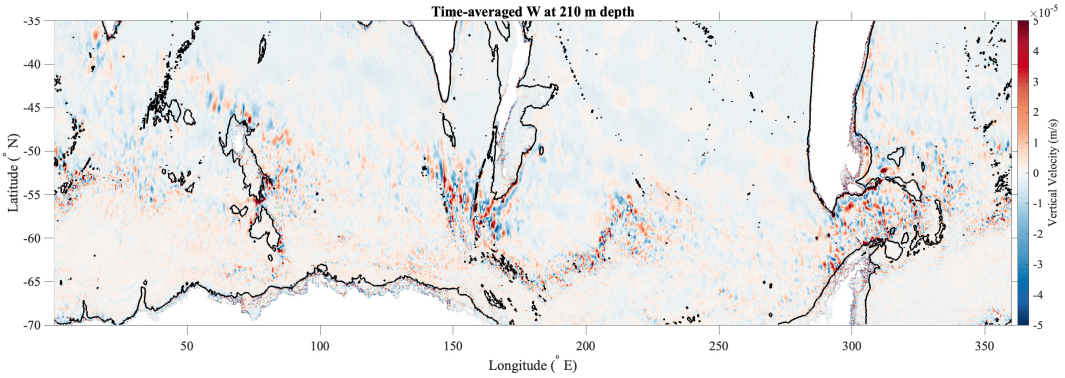

Figure 1. A figure showing the vertical velocities at 210 m depth in the Southern Ocean State Estimate (SOSE) 1/6 degree simulation averaged from 2013 to 2018. The black contours show the 2000 m isobath showing the location of topography. This shows us that the vertical velocities are not uniform across the Southern Ocean, but enhanced near topographic features, countering the assumption of residual overturning theory that the circulation is uniform throughout the Southern Ocean.

& Gnanadesikan, 2006; R. Abernathey et al., 2011; Meredith et al., 2012). It is hypothesized that as the wind strengthens, the wind driven overturning strengthens and the isopycnal slopes steepen, leading to an increase in the eddy driven circulation, at least partially compensating for the change in the wind driven circulation (Marshall & Speer, 2012). However this is based on the zonally symmetric conception of the overturning (R. Abernathey et al., 2011), so little is know how the topography changes sensitivity of the overturning. There have been several studies about the sensitivity of the overturning to changes in wind with topography, but with limited results (Meredith et al., 2012; Zhai & Munday, 2014; Munday & Zhai, 2015; Bishop et al., 2016). There is still a gap with connecting the flat bottomed theory to how the sensitivity is different with a ridge and without.

The Southern Ocean State Estimate shows that vertical velocities are isolated near topography (Figure 1), suggesting the importance of the topography for driving upwelling. This has been confirmed in similar models by showing particle upwelling localized to regions downstream of topography (Tamsitt et al., 2018; Viglione & Thompson, 2016). The localized upwelling has been suggested to be due to baroclinic eddies enhanced downstream of topography. In addition, studies have shown that Antarctic Intermediate Water and Antarctic Bottom Water are formed locally (Talley, 2013). However, there is a gap in understanding how this picture connects to the zonally symmetric theory of the overturning. In this paper, we will address this by showing specifically which processes are leading to the vertical transport of water in which locations.

In this study, we use an MITgcm channel model representing the Antarctic Circumpolar Current, with idealized geometry and forcings, to understand how three-dimensionality of the geometry leads to three-dimensionality of the flow. We build off a two-layered simulation with similar parameters in Youngs et al. (2019) and an MITgcm set-up with a similar framework (Youngs et al., 2017). In this paper, we describe the numerical model in section 2. In section 3, we investigate the three-dimensionality of the flow and the driving forces behind it. In section 4 we investigate the response of the overturning to changes in wind. In section 5 we present two considerations in applying these results to more complex models. In section 6 we discuss and conclude.

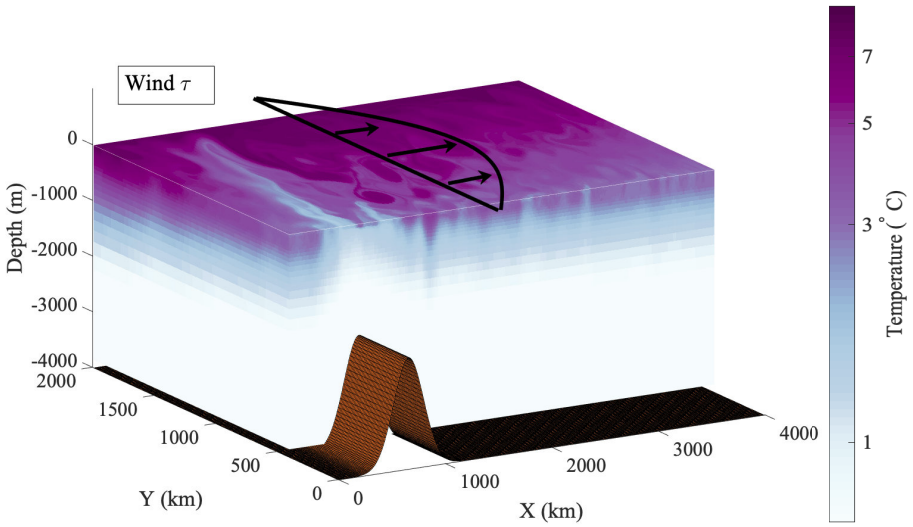

Figure 2. Geometry of the idealized MITgcm channel. There is a Gaussian ridge that is 2000 m tall located at 800 km, wind has a cosine profile with a maximum τ_0, the color here is a snapshot temperature with $\tau_0 = 0.15$ N m^{-2}. The ridge is a similar dimension and steepness compared to real topographic features in the Southern Ocean and the channel length approximates the spacing of major topographic features.

2 Ocean Model

We use an MITgcm channel that is 4000 km long by 2000 km wide and re-entrant in longitude (Figure 2). The model is run at a 10 km resolution. The deformation radius in this configuration is about 15 km, but features tend to be larger than the deformation radius (Pedlosky, 1987). As a check, we also ran the simulations at a 5 km resolution and saw the same physical behavior. We have a total depth of 4000 m with 32 points in vertical, from 10 m grid spacing at the surface to 280 meters in grid spacing at the bottom, as used in previous studies (R. Abernathey et al., 2011; Youngs et al., 2017). For topography we have a Gaussian ridge of half-width 200 km, 2000 m tall, located at 800 km downstream of the channel entrance (Figure 2). We use a 600 second time step, free slip sides, and a diffusivity varying from 0.01 m^2 s^{-1} to 1×10^{-5} m^2 s^{-1} with a tanh profile with a decay scale corresponding to a mixed layer depth of 40 m. We also have a linear bottom drag with a drag coefficient of 1.1×10^{-3}m s^{-1}. We note here that we split up the domain into three regions: the upstream region ahead of the topography, the downwash region from 800 km to 2000 km, and the downstream region, 2000 km to the end of the domain. We choose this idealized geometry because it is the simplest configuration that has a three-dimensional, zonal-asymmetry like seen in the Southern Ocean.

2.1 Boundary Conditions

The surface is forced using a wind stress of the form

$$\tau(y) = \tau_0 \sin(\pi y / L_y) \tag{1}$$

where $L_y = 2000$ km. For the base case, $\tau_0 = 0.15$ N/m^2; it will be varied from 0.05 to 0.25 N/m^2 (Figure 2).

At the northern boundary, the temperature (which determines the buoyancy) relaxes to a fixed profile with a timescale of 1 week, as an exponential profile

$$T_n(z) = \Delta T(e^{z/z'} - e^{-H/z'})/(1 - e^{-H/z'}) \tag{2}$$

where T_n is the temperature at the northern boundary, H is the domain depth of 4000 m, and $-z'$ is a decay depth of 1000 m. The choice of profile is justified by Karsten and Marshall (2002).

We use a surface relaxation condition because it allows the strength of the overturning to change as we change the wind. We note here that the overturning does change with changes in wind stress with a fixed flux, however the effect is smaller. Using a fixed surface relaxation temperature profile for both the flat bottom and ridge cases leads to wildly different overturnings; instead we have adopted a method which allows both a relaxation boundary condition and comparable overturnings for the flat bottom and ridge simulations. We first run simulations with a fixed flux surface boundary condition as shown in Figure 3(b) for both ridge and flat-bottomed cases. From these simulations, we use the time- and zonally-averaged surface temperature to choose a relaxation temperature profile $T_0(y)$ with a heat flux $Q = -\lambda(\langle T \rangle - T_0)$ where λ is the relaxation time scale of one month and T_0 is the temperature profile calculated. The time scales and procedure is developed after R. Abernathey et al. (2011). In other words, we ran one flat and one ridge simulation to set the temperature relaxation profiles, then fixed the relaxation profiles in the wind perturbation experiments. This creates comparable overturning circulations as seen in Figure 4. This method of using the fixed flux conditions in order to generate a temperature relaxation is required because the isopycnal slopes are very different between these two cases. The heat fluxes are not zonally symmetric and are visibly enhanced near topography due to colder water being brought northward (Figure 3(d)).

2.2 Particle tracking

We are going to examine the spatial distribution of upwelling and downwelling, as well as determining the relative importance of the mean and the eddies, by tracking particles in the thickness weighted mean velocity. The computation is done using standard Lagrangian equations for movement in a specified flow field. To understand why using this is appropriate with the thickness-weighted mean velocities, consider solving the passive tracer equation

$$\frac{\partial}{\partial t}\theta + \tilde{\mathbf{u}} \cdot \nabla\theta = 0 \tag{3}$$

with a delta function initial condition

$$\theta = \delta(\mathbf{x} - \mathbf{X}(t)) \tag{4}$$

where $\mathbf{X}(t)$ gives the particle position. Particles generally stay on buoyancy surfaces; those that do not because of diabatic processes in the surface layer or interpolation errors are discarded. Thus, the vertical velocities calculated here are purely adiabatic and along isopycnals.

We use the thickness-weighted horizontal and vertical velocities $\tilde{\mathbf{u}} = \mathbf{u}^\sharp(\mathbf{x}, t)$ as defined by Young (2012). This choice was made because the mean velocities are not parallel to the mean buoyancy surfaces (the Reynolds' heat fluxes imply that $\overline{u}\cdot\nabla\overline{b} \neq 0$), and, therefore, using them to advect particles would not represent the upwelling and downwelling properly. In contrast, the thickness-weighted velocities ensure that the particles stay on the mean buoyancy surfaces. The thickness weighted average is

$$\hat{\theta} = \frac{\overline{\theta h}}{\overline{h}} \tag{5}$$

where h is the thickness of a layer defined by $d^3\mathbf{x} = dx\,dy\,dz = h\,d\tilde{x}\,d\tilde{y}\,d\tilde{b}$, where the $\tilde{}$ indicate buoyancy coordinates. The overbar represents a time-average. Properties are

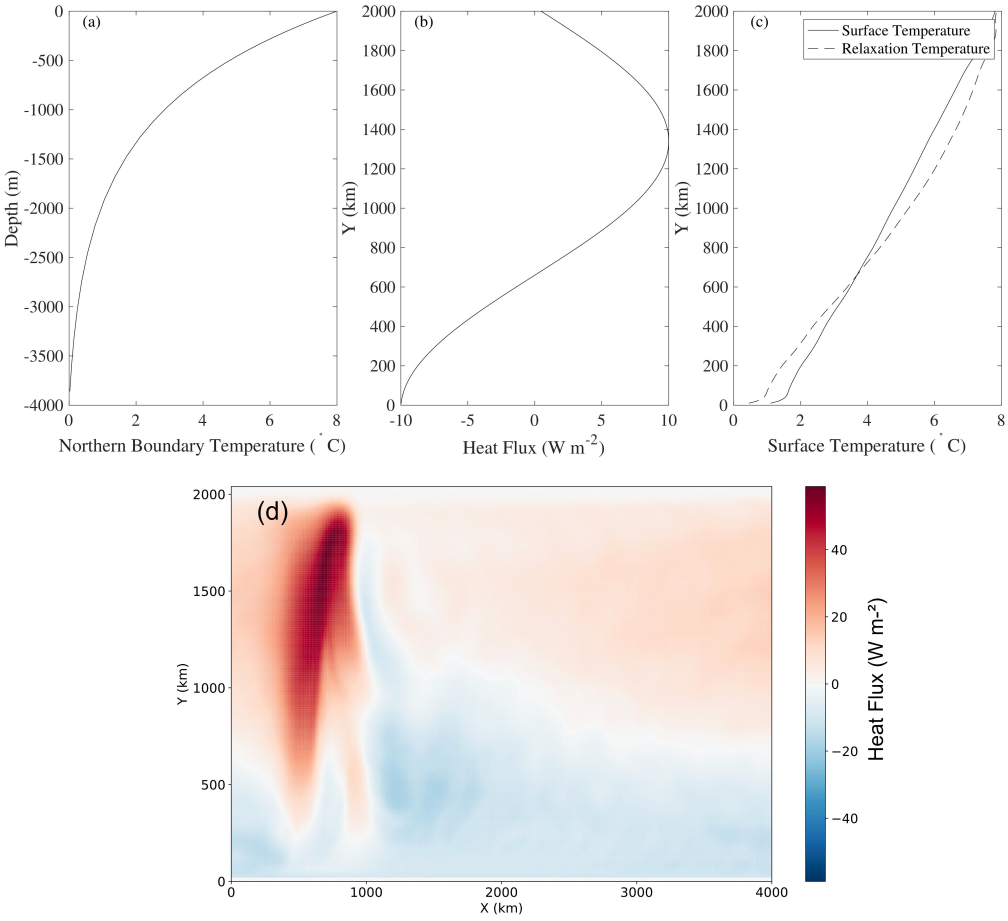

Figure 3. Figure showing the temperature boundary conditions. (a) Northern boundary relaxation temperature. The temperature is relaxed linearly from the maximum at the northern boundary, linearly scaling back to no forcing at 1930 km. (b) Heat flux profile used with the average surface temperature (c) to generate surface relaxation temperature. (d) shows the full heat flux pattern for $\tau_0 = 0.15$ N m^{-2}. From these forcings, we generate an upper and a lower overturning cell of reasonable strength relative to the channel length.

interpolated to buoyancy (equivalent to temperature) surfaces, multiplied by the instantaneous thicknesses, h, and then time-averaged. The height of the buoyancy surface is given by

$$z = \zeta(\tilde{x}, \tilde{y}, \tilde{b}, \tilde{t}) \tag{6}$$

where ζ defines the buoyancy surface. The three-dimensional residual is given by

$$\mathbf{u}^\sharp = \left(\frac{\overline{hu}}{\overline{h}}\,,\ \frac{\overline{hv}}{\overline{h}}\,,\ \frac{\overline{hu}}{\overline{h}}\,\overline{\zeta}_{\hat{x}} + \frac{\overline{hv}}{\overline{h}}\,\overline{\zeta}_{\hat{y}} \right) \tag{7}$$

The $\hat{x}$, $\hat{y}$ derivatives are taken in buoyancy space. The advective derivative for θ looks the same as usual, but with the $\mathbf{u}^\sharp$ velocities.

The contribution to the vertical displacement from the eddies is simply the difference between advection by the Eulerian-mean $\overline{\mathbf{u}(\mathbf{x})}$ and by the thickness-weighted mean $\mathbf{u}^\sharp(\mathbf{x})$. We use the "layers" package to calculate $\overline{uh}, \overline{vh}, \overline{h}, \overline{u}, \overline{v}$ on temperature layers or in $(\tilde{x}, \tilde{y}, \tilde{b}, \tilde{t})$-coordinates. The time-averaged temperatures are used to calculate $\overline{\zeta}_{\tilde{x}}$ and $\overline{\zeta}_{\tilde{y}}$. The thickness-weighted averages $\hat{u}$, $\hat{v}$, $\overline{\zeta}_{\tilde{x}}$, and $\overline{\zeta}_{\tilde{y}}$ are transformed back into (x, y, z, t)-coordinates. From this we calculate $\mathbf{u}^\sharp$ and export these velocities so that particles can be released and tracked in the thickness-weighted velocity field.

2.3 Overturning Calculation

We then can calculate the residual overturning as follows:

$$\psi = \int_0^{T'} \int_0^{x_{max}} \overline{vh} dx dT \tag{8}$$

where h is the temperature (buoyancy) layer thickness, v is the meridional velocity in the layer. We show the meridional overturning circulation for both the flat bottom and ridge cases (Figure 4). The simulations with a ridge show an extra feature in the overturning due to the surface heat fluxes associated with the meandering flow. This is shown by the blue, negative cell entirely within the envelope of temperatures seen at the surface. When this overturning is then projected into depth-space, the surface meander feature is projected below the surface ocean, misleading the reader by showing a non-existent diabatic process at depth. A meander here is a north/south deviation of flow in the time-mean. The vertical isopycnal seen in Figure 4(d) is an artifact of the meander as well, because that colder temperature reaches the surface only over the topography. One difference between the flat-bottom and the ridge simulations is the steepness of the isopycnal slopes. They are much steeper for the flat-bottomed simulations, leading the lower cell to be much deeper in the domain than with the ridge simulations (R. P. Abernathey & Cessi, 2014). This has implications for which water masses reach the surface and where they are exchanged with the rest of the ocean.

As a note for further analysis, we split up overturning cells based on temperature ranges as seen in figure 4. The lower cell downwelling is the coldest temperatures seen to the maximum in the lower cell overturning as seen close to the northern boundary. The lower cell upwelling is the temperature range between the maximum of the lower cell and the sign change of the overturning, again along the northern boundary. The upper cell upwelling is defined by the temperature range from the sign change to the maximum of the overturning seen at the northern boundary.

3 Three-dimensional Circulation

3.1 Method

In order to visualize the three-dimensional flow, we use particle tracking in the thickness-weighted flow. We release particles $x = 100$ km and every y and z location on the na-

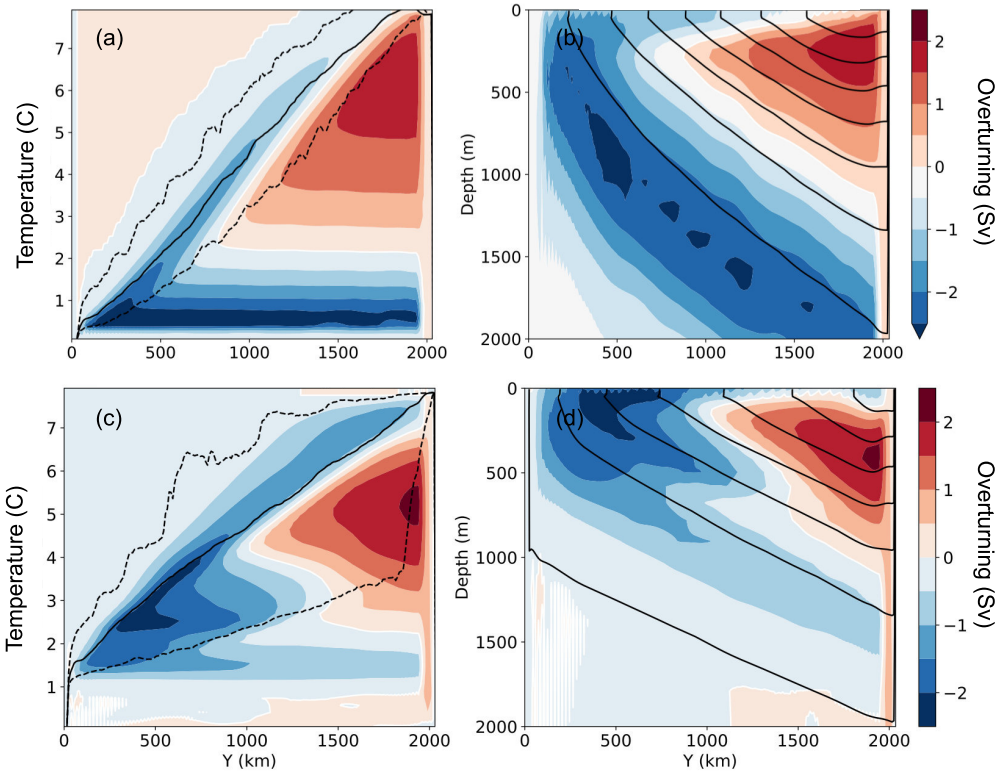

Figure 4. Residual overturning in temperature space (a,c). The same overturning projected into depth coordinates (b,d). The overturning is shown for flat-bottomed simulations (a,b) and ridged simulation (c,d). The solid black line shows the mean surface temperature versus Y, and the dashed lines show the 1 and 99 percentile of temperature values, representing the temperatures exposed to the surface. These show similar overall magnitude of the residual overturning for both flat-bottomed and ridge simulations, but with an additional feature in the lower cell in the ridge simulations due to the meandering flow over topography.

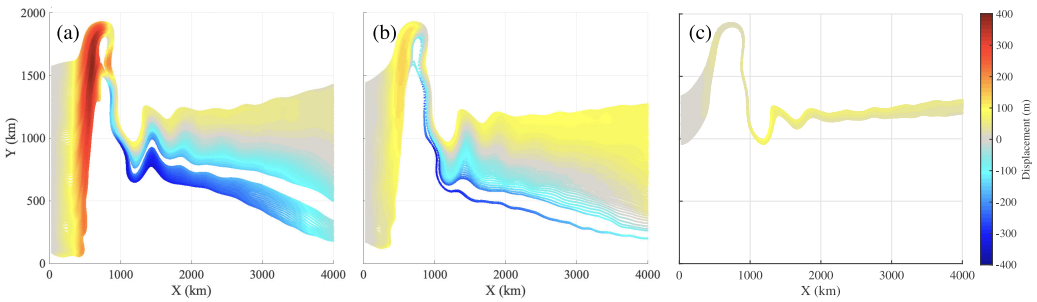

Figure 5. A figure showing the residual displacement on three different temperature surfaces, representing the three different overturning branches that we can resolve. We release particles at the western boundary of the domain and follow them to calculate their displacement relative to their initial z positions. (a) shows particles released at 1 C, which represents lower cell downwelling. (b) shows particles release at 2 C which represents lower cell upwelling. (c) shows particles released at 4 C which represents upper cell upwelling. The upwelling and downwelling seen here is reflective of that seen in Figure 4. Particles move north and south due to the ridge and experience different vertical transport depending on their location.

tive grid, near the entrance to the channel. We advect the particles using an RK-2 advection scheme in the thickness-weighted velocities. We discard particles that enter the mixed layer, and those that enter the northern temperature relaxation region. We analyze the particles based on the initial temperature and eliminate particles if they change temperature too much (± 0.1 C). This range was chosen arbitrarily, however changing the range does not affect the results. In addition, we tabulate the vertical displacement from just the Eulerian mean in depth space in order to produce an eddy versus mean displacement. The particles are still advected in x, y, z using the full thickness-weighted flow, but the vertical displacement is calculated with the local mean w by multiplying by the time step and adding it to calculate the mean displacement. We show the vertical displacement following these particles in figure 5. We see that the particles go up and down over the topography and then generally see enhanced upwelling downstream of the topography, in the downwash region, and then a leveling out far downstream. The upwelling and downwelling seen in these chosen temperature layers is reflective of the overturning circulation calculated for figure 4.

We average over the latitudes (Y) in each temperature layers to understand the cumulative upwelling versus position down the channel, allowing a visualization of the upwelling surface and splitting the components into mean and eddy (Figure 6). The vertical displacement is divided by the total time it takes to transit the domain, in part because the total displacement in one transit of the channel is much larger for the colder temperature layers because the transit time is much slower. Dividing by the mean total time of each temperature layer allows a clearer comparison between the different temperature layers.

3.2 Eulerian Mean Versus Transient Eddies

We investigate the cumulative vertical displacement on temperature surfaces of particles as they transit the domain west to east (Figure 6). The total upwelling has a very localized pattern with peaks located near the topography and in the downwash region at 1200 km (Figure 6a). By the end of the domain, we see the upwelling and downwelling we expect by looking at the meridional overturning (Figure 4). We compare this to the

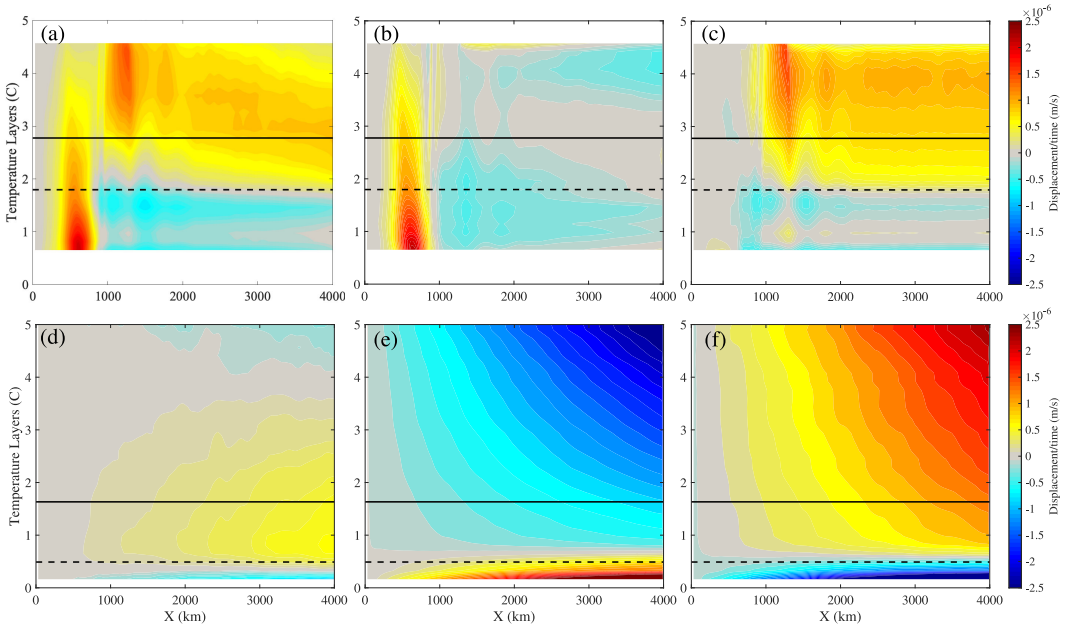

Figure 6. An analysis of the displacement of particles for a ridge case (a,b,c) and a flat bottom (d,e,f). We then split up the flow from the total residual (a,d) into the mean (b,e) and eddies(c,f), where the vertical advection of each component is catalogued separately. The displacement is normalized by the total amount of time to transit throughout the domain. This shows us that the transient eddies are localized strongly in the downwash region (X = 1000 km), although the mean component is leading order for the lower cell upwelling. For ridge, total isn't a small residual between the winds and the other components.

total upwelling with a flat bottom (Figure 6d) which shows us the same pattern but with a purely linear increase, indicating the zonally symmetric nature of the flat-bottomed simulations. Also for the flat bottom, the mean (e) and the eddies (f) have opposing signs so that the total is a small residual. This method reproduces the results of the well-studied zonally symmetric system, giving us confidence in the robustness of our analysis.

For the ridge case, most of the structure comes from the area right around the ridge (Figure 6b). Since the mean is not primarily zonally symmetric, most of the signal we are seeing is from what we can call the standing eddy component. You can see the effects of the wind-driven zonally-symmetric component in the downwash regions by the linearly changing patterns. The eddies (Figure 6c), on the other hand are localized in the downwash region, where they lead to upwelling or downwelling in one location and then nothing changes the rest of the domain. Thus, the lower cell downwelling is driven by the eddies and the mean, where as the lower cell and upper cell upwelling is primarily driven by the transient eddies. Thus, each cell is driven by different processes, which has implications for how the overturning changes with the wind stress.

3.3 Understanding the Eulerian Mean Overturning

From Figure 6, the pattern of the mean vertical transport seems to have multiple components, one localized near the topography and one linearly changing throughout the domain. To further investigate this, we split the Eulerian advection into Ekman velocities and the remainder. The Ekman velocities are calculated using the wind-stress

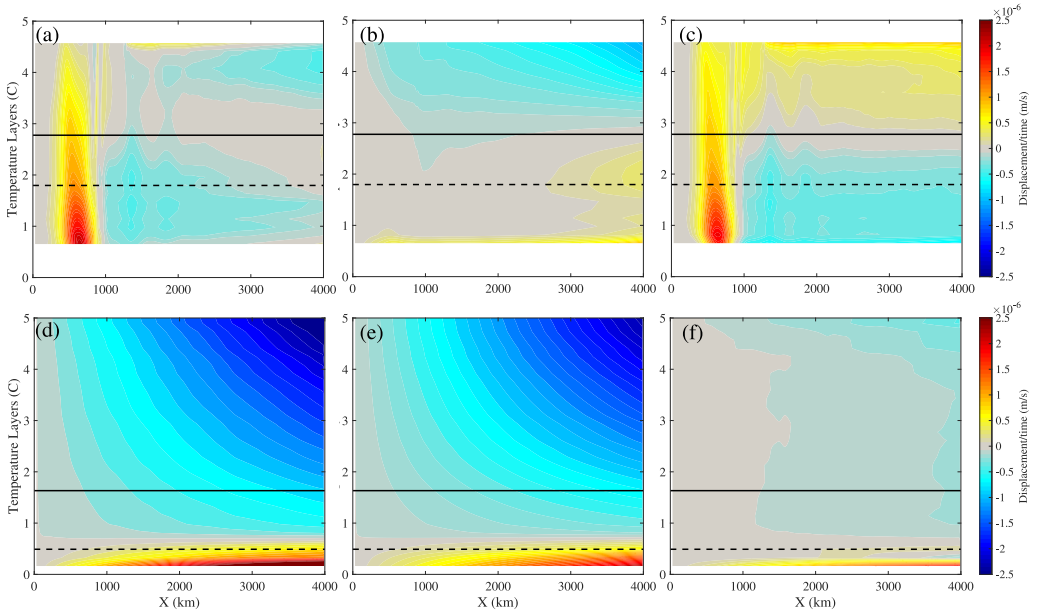

Figure 7. An analysis of the Eulerian-mean displacement of particles for a ridge case (a,b,c) and a flat bottom (d,e,f). We then split up the flow from the mean displacement (a,d) into the Ekman (b,e) and standing eddy(c,f), where the vertical advection of each component is catalogued separately. The displacement is normalized by the total amount of time to transit throughout the domain. The Ekman component is dominant in the upper cell upwelling whereas the standing eddy component is dominant in the lower cell. Standing eddies primarily act in the downwash region.

curl forcing and we assume they are the same at every depth. This is a fair assumption because the scale depth of the ocean is much deeper than the ocean bottom. This assumption is validated in the flat bottomed case where almost all the Eulerian velocities are Ekman velocities (Figure 7).

For the flat bottom, as expected, the difference between the mean and the Ekman flow is small, validating the metric. For the ridge, on the other hand, there are two components, a weak Ekman term that results in approximately uniform upwelling across the domain. This is likely weak due to the north-south movement of particles in this case and flat isopycnals allowing more cancellation of negative and positive Ekman velocities. The second component is a standing eddy component with a big rise and fall over the topography, then a rise in the warmer waters and a fall in the cooler ones. The ridge even modifies how the winds affect the overturning particles, so that all components of the overturning are modified by the topography.

This standing eddy component has been shown to be an important part of the overturning circulation. The standing eddy component is determined by examining the time-mean overturning that is a deviation from the zonal average and then taking a zonal average to analyze. Many different studies in realistic geometries highlight the role of this component and its leading order nature (Bishop et al., 2016; Dufour et al., 2012). We again find this to be the leading order of the overturning.

4 Sensitivity to Wind

The most salient implication for this localized understanding of the overturning circulation is in the sensitivity of the overturning to changes in wind. Figure 8 shows how the overturning strength changes as the wind stress increases or decreases for both a flat bottomed simulations and ridged simulations. We see that the sensitivity to the wind stress is very similar for the upper cell for both flat and ridge cases, but the lower cell is a different story. With a ridge, the lower cell overturning hardly changes at all as the wind changes, unlike with a flat bottom. Thus, the topography significantly alters the sensitivity of the overturning. In this section we provide a first direct comparison between ridge and flat bottom Southern Ocean channels overturning and connect the underlying dynamical processes.

4.1 Isopycnal Slope Changes

In the lower cell, the magnitude of the overturning is controlled primarily by the magnitude of the surface buoyancy flux. The temperature range of the lower cell barely outcrops at the surface in the time mean, so Ekman pumping can hardly act to drive overturning for the lower cell. For the upper cell, Ekman pumping also plays a role, somewhat complicating the picture. However for both cases, the magnitude of the buoyancy flux is then controlled by the temperature difference between the surface and relaxation temperature. Since the isopycnals are essentially pinned at the northern boundary due to the quick relaxation time scale, the surface outcrops are a reflection of the isopycnal slopes. This allows us to connect how the isopycnal slopes vary to changes in the overturning.

We have examined how the isopycnal slopes change in both upper and lower overturning cells in a two-layer quasi-geostrophic channel (Youngs et al., 2019). This study can help us interpret how the isopycnal slopes are changing in our channel (Figure 8). Essentially for the lower cell ridge case, we are seeing very little change in the isopycnal slopes with changing wind, which is in agreement with the response of the weakly negative overturning in the two-layer quasi-geostrophic study. This is very different for the flat bottom where the isopycnal slopes get steeper in both ridge and flat bottom, also in agreement with the quasi-geostrophic model. The system transitions from a state with a very small meander due to the small barotropic component of the flow to one with a large meander due to a larger barotropic component. This transition is what results in the particular isopycnal slope distributions with wind. This is due to localization of the eddy activity near the topography (MacCready & Rhines, 2001; Youngs et al., 2017, 2019). Thus we can use our understanding of why the slopes change the way they do from the quasi-geostrophic model and apply it to our more realistic modeling.

As we show in Youngs et al. (2019), this change of sensitivity is due to the fundamentally different response of the lower cell to the wind when there is a ridge: in that case, as the winds increase, the system transitions from a bottom-insensitive configuration, dominated by buoyancy fluxes, to the bottom-sensitive configuration dominated by the winds. As the winds strengthen the flow becomes more barotropic and the surface flow is more and more affected by the topography. We provide a new plausible explanation for why the overturning changes with wind as it does.

4.2 Dynamical Processes

We have made an argument for why the isopycnal slopes change with changes in wind and how that changes the surface buoyancy fluxes. There is still a remaining gap here about which dynamical components of the overturning respond to changes in wind. In eddy permitting models, several studies find that the standing eddies absorb the changes in the wind (Dufour et al., 2012; Bishop et al., 2016). In addition, standing eddies have

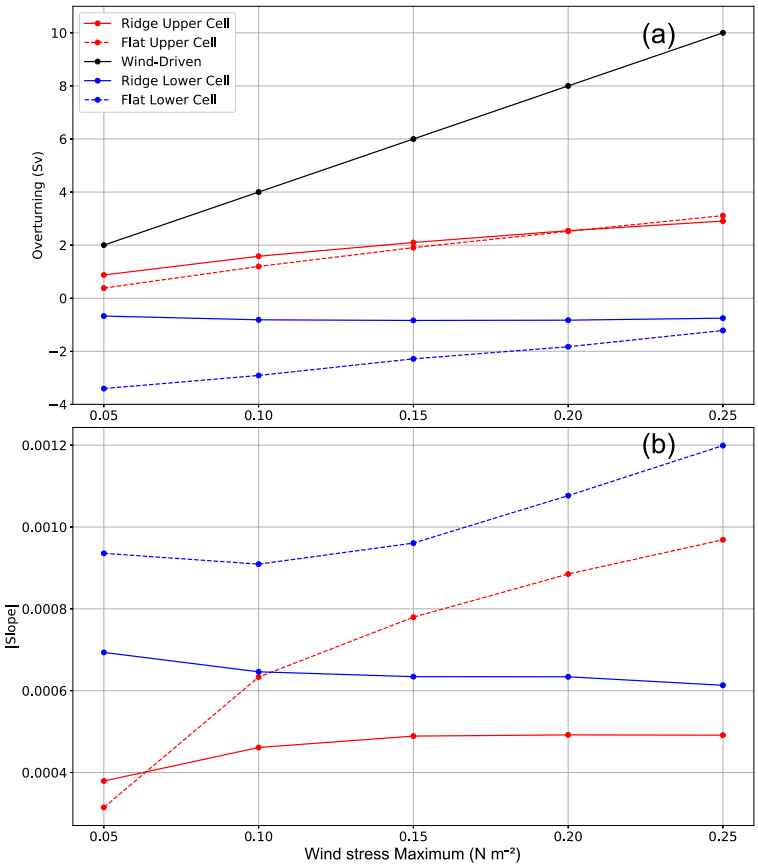

Figure 8. This figure shows the overturning versus the wind stress maximum for both the flat-bottomed and the ridged simulations (a) and the slopes for each cell (b) averaged over 40 years. We show here that the sensitivity is much weaker for the lower cell when we have topography indicating that the zonal asymmetry (the ridge) is important for the sensitivity. The change in overturning is in part understood by the changes in isopycnal slopes, whose response is studied in detail in Youngs et al. (2019).

been shown to sharpen to respond to changes in wind stress (Thompson & Naveira Garabato, 2014). A similar analysis could and should be done with the methods shown here, but are outside the scope of this paper.

The standing eddy component is especially important in the lower cell, which effectively absorbs changes in the wind. Therefor it is consistent that there would be little change in the overturning with changes in wind. On the other hand, the processes driving the upper cell are more similar to the flat bottom with a wind stress balanced by transient eddies, so the upper cell's response to the wind for a ridge is similar to the flat bottom. Thus it seems that the differing driving processes in the upper and lower cell have different sensitivities to the wind, meaning that all three components of the overturning's sensitivity need to be modeled correctly in order to produce an appropriate overall sensitivity.

5 Metrics for Evaluating Models

5.1 Localized Enhanced Diffusivities

The localization of eddies just downstream of the ridge is very important for how the system responds to winds. The enhanced local eddy activity is responsible for the way the isopycnal slopes respond to changes in wind. In addition, the enhanced localized eddy activity is also evident with eddy-driven upwelling localized near the topography (Figure 6). The enhanced local eddies are also evident in observations and more realistic models (Hogg et al., 2015; Bishop et al., 2016). This enhanced eddy activity leads to elevated eddy diffusivities near the topography (R. P. Abernathey & Cessi, 2014; Sallee et al., 2011).

Since the local eddy activity and thus localized enhanced eddy diffusivities are fundamentally important in setting how the system responds to changes in forcing, it is consistent that the local diffusivities would be an important factor in sensitivity. In a comprehensive review of modeling studies examining how the overturning changes with wind, Gent (2016) finds that model configurations where the Gent-McWilliams parameters were allowed to vary in latitude and longitude are less sensitive to changes in wind. This is because the localization of the eddy activity is parameterized by the localized Gent-McWilliams diffusivity. This suggests a way forward to make sure climate models appropriately respond to changes in wind stress.

5.2 Three-dimensional Signatures in Zonally Averaged Diagnostics

Now that we have demonstrated the three-dimensional structure to the overturning, we ask if it is possible to see this signature in the standard zonally-averaged diagnostics. We show in Figure 9 the overturning calculation split into the Eulerian mean and the eddy components for the flat bottomed and ridge cases. We note that for the ridge case, the total in this zonally averaged framework is a small residual of the Eulerian-mean and eddy components, in contrast to the particle tracking diagnostics where the total, Eulerian-mean, and eddy components all being the same magnitude (Figure 6). The main differences between the ridge and flat cases are the vertically-banded features in the Eulerian mean and the depth of the overturning.

This leaves the question, why is the Eulerian-mean component so much smaller, relatively, for the particle tracking diagnostics. We suggest that this is due to the particles traveling north and south throughout the domain experiencing the Ekman velocities in varying degrees depending on their position in y. In addition we are averaging over y in a temperature layer, leading to partial cancellation in the north and south. This effect is larger for the ridge case because of the flatter isopycnals. Thus there is relatively little signal of the zonal-asymmetry in the overturning when diagnostics are performed

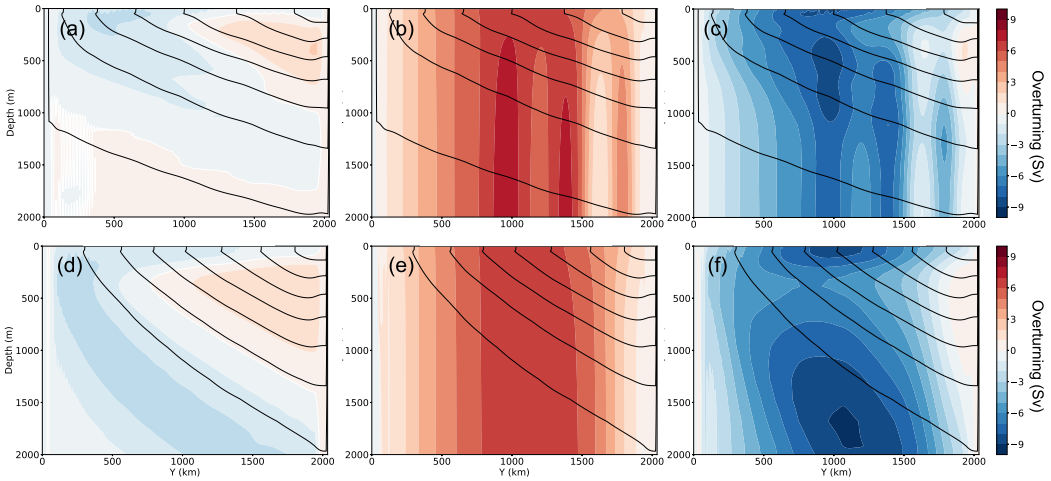

Figure 9. The meridional overturning (a,d) split up into Eulerian mean (b,e) and eddy (c,f) components for the ridge (a,b,c) and flat bottom (d,e,f) cases. This shows us that the zonally averaged diagnostics don't show many signatures of the localization, and over-estimate the contribution of wind-driven overturning.

with a zonal-averaged. This highlights the need for caution when analyzing the Eulerian mean overturning because it over-represents the role of the wind-driven overturning. Calculating the mean overturning on isopycnals instead, may produce more fruitful results and the split into standing and transient eddies may bring more results (e.g. Bishop et al., 2016; Viebahn & Eden, 2012).

6 Discussion and Conclusions

Throughout this study, we have connected localized particle upwelling to the thickness-weighted averaged circulation theory using an idealized Southern Ocean-like channel. We have shown that the zonally symmetric residual overturning is an inaccurate picture because of the localized nature of the overturning (Figure 10). The topography dramatically reduces the sensitivity of the lower cell overturning to changes in wind. This is a related to how the isopycnal slopes evolve with the wind (Youngs et al., 2019). Including the topography is essential for predicting the sensitivity, in agreement with studies that show that the standing meander is primarily responding to changes in wind (Dufour et al., 2012; Bishop et al., 2016).

We improve our understanding of the Southern Ocean by extending the zonally-symmetric picture to three-dimensions with thickness-weighted circulation. We also show definitively that upwelling near topography is in fact driven by predominantly transient eddies. We also provide a physical explanation for why the overturning changes the way it does with wind when there is a ridge, providing clarity to the discussion of eddy compensation, where it is likely that standing eddies absorb much of the change of the wind. In addition, a word of caution is given using zonally-averaged diagnostics, because they over-represent the role of wind-driven transport in the channel with topography.

One limitation to generalizing these results is the idealized geometry. This idealized geometry allows for a clear picture of the overturning while also leaving open the question of how our study generalizes to the topographic configuration of the Southern Ocean. While we expect our results to apply to a more realistic geometry, more investigations are necessary to tie the theory to the circulation. Another particular caveat con-

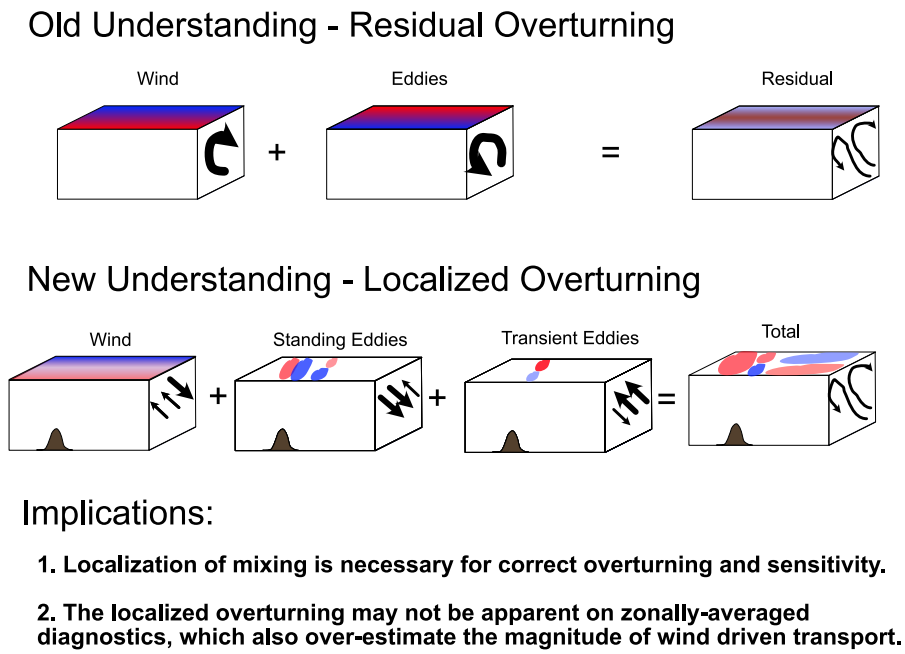

Figure 10. This figure schematically shows how our understanding of the overturning circulation changes with the addition of a zonal asymmetry due to topography. The new understanding highlights the role of the time-mean circulation via the standing eddy as a leading order feature of the residual overturning circulation, as well as the localized nature. A reduction in sensitivity to changes in wind is experienced by the lower cell, due to this localized nature.

cerning the Southern Ocean lower cell. In the ocean, Antarctic Bottom Water occurs primarily at two very localized places, the Weddell and Ross seas (Talley, 2013; Rintoul, 2018). We do not replicate that localization or the specific overflow processes that generate the water mass. This amount of specificity and detail was outside the scope of this project, but we suggest to do a similar analysis in more complex models that represent these processes.

Our study emphasizes that localization is fundamental for the global overturning, but we remark that this localization is also fundamental for where carbon and other tracers upwell into the mixed layer. As highlighted in Youngs (2020), we also see that this leads to very specific patterns of carbon outgassing. This suggests the necessity of highly-localized in situ measurements above topography to appropriately sample the carbon budget and vertical transport in the Southern Ocean. We now have a better dynamical understanding of the relevant overturning processes in the three-dimensional Southern Ocean and can now analyze the three-dimensional circulation in more complex models using the method outlined here.

Acknowledgments

We acknowledge helpful discussions with Mara Freilich, Andrew Stewart, David Marshall, Nikki Lovenduski, and Mike Spall. MKY acknowledges funding from the National Defense Science and Engineering Graduate Fellowship and the NOAA Climate and Global

Change Postdoctoral Fellowship and NSF OCE-1536515. GRF acknowledges funding from NSF OCE-1459702. The code used to run the model is available at https://zenodo.org/badge/latestdoi/363190132

References

Abernathey, R., Marshall, J., & Ferreira, D. (2011, dec). The Dependence of Southern Ocean Meridional Overturning on Wind Stress. *Journal of Physical Oceanography*, *41*(12), 2261–2278. Retrieved from `http://journals.ametsoc.org/doi/10.1175/JPO-D-11-023.1` doi: 10.1175/JPO-D-11-023.1

Abernathey, R. P., & Cessi, P. (2014). Topographic Enhancement of Eddy Efficiency in Baroclinic Equilibration. *Journal of Physical Oceanography*, *44*(8), 2107–2126. doi: 10.1175/JPO-D-14-0014.1

Bishop, S. P., Gent, P. R., Bryan, F. O., Thompson, A. F., Long, M. C., & Abernathey, R. P. (2016). Southern Ocean Overturning Compensation in an Eddy-Resolving Climate Simulation. *Journal of Physical Oceanography*, *46*(5), 1575–1592. doi: 10.1175/JPO-D-15-0177.1

Dufour, C. O., Le Sommer, J., Zika, J. D., Gehlen, M., Orr, J. C., Mathiot, P., & Barnier, B. (2012). Standing and transient eddies in the response of the southern ocean meridional overturning to the southern annular mode. *Journal of Climate*, *25*(20), 6958–6974.

Frölicher, T. L., Sarmiento, J. L., Paynter, D. J., Dunne, J. P., Krasting, J. P., & Winton, M. (2015, jan). Dominance of the Southern Ocean in anthropogenic carbon and heat uptake in CMIP5 models. *Journal of Climate*, *28*(2), 862–886. Retrieved from `http://journals.ametsoc.org/doi/10.1175/JCLI-D-14-00117.1` doi: 10.1175/JCLI-D-14-00117.1

Gent, P. R. (2016). Effects of southern hemisphere wind changes on the meridional overturning circulation in ocean models.

Gruber, N., Gloor, M., Mikaloff Fletcher, S. E., Doney, S. C., Dutkiewicz, S., Follows, M. J., ... Takahashi, T. (2009, mar). Oceanic sources, sinks, and transport of atmospheric CO2. *Global Biogeochemical Cycles*, *23*(1), n/a–n/a. Retrieved from `http://doi.wiley.com/10.1029/2008GB003349` doi: 10.1029/2008GB003349

Hallberg, R. W., & Gnanadesikan, A. (2006). The Role of Eddies in Determining the Structure and Response of the Wind-Driven Southern Hemisphere Overturning: Results from the Modeling Eddies in the Southern Ocean (MESO) Project. *Journal of Physical Oceanography*, *36*(12), 2232–2252. Retrieved from `http://journals.ametsoc.org/doi/pdf/10.1175/JPO2980.1http://journals.ametsoc.org/doi/abs/10.1175/JPO2980.1` doi: 10.1175/JPO2980.1

Hogg, A. M., Meredith, M. P., Chambers, D. P., Abrahamsen, E. P., Hughes, C. W., & Morrison, A. K. (2015, jan). Recent trends in the Southern Ocean eddy field. *Journal of Geophysical Research: Oceans*, *120*(1), 257–267. doi: 10.1002/2014JC010470

Karsten, R. H., & Marshall, J. (2002). Testing theories of the vertical stratification of the Antarctic Circumpolar Current against observations. *Dynamics of Atmospheres and Oceans*, *36*(1–3), 233–246.

Le Quéré, C., Andrew, R. M., Friedlingstein, P., Sitch, S., Pongratz, J., Manning, A. C., ... Zhu, D. (2017). Global Carbon Budget 2017. *Earth System Science Data Discussions*, 1–79. Retrieved from `https://www.earth-syst-sci-data-discuss.net/essd-2017-123/` doi: 10.5194/essd-2017-123

MacCready, P., & Rhines, P. B. (2001). Meridional Transport across a Zonal Channel: Topographic Localization. *Journal of Physical Oceanography*, *31*(6), 1427–1439. doi: 10.1175/1520-0485(2001)031⟨1427:MTAAZC⟩2.0.CO;2

Marshall, J., & Speer, K. (2012). Closure of the meridional overturning circulation through Southern Ocean upwelling. *Nature Geoscience*, *5*(3), 171–180. Re-

trieved from http://oceans.mit.edu/JohnMarshall/wp-content/uploads/2013/08/Closure-of-the-meridional-overturning{_}134.pdfhttp://www.nature.com/doifinder/10.1038/ngeo1391 doi: 10.1038/ngeo1391

Meredith, M. P., Naveira Garabato, A. C., Hogg, A. M., & Farneti, R. (2012). Sensitivity of the overturning circulation in the Southern Ocean to decadal changes in wind forcing. *Journal of Climate*, *25*(1), 99–110. Retrieved from http://journals.ametsoc.org/doi/pdf/10.1175/2011JCLI4204.1 doi: 10.1175/2011JCLI4204.1

Munday, D. R., & Zhai, X. (2015). Sensitivity of Southern Ocean circulation to wind stress changes: Role of relative wind stress. *Ocean Modelling*, *95*, 15–24. Retrieved from http://dx.doi.org/10.1016/j.ocemod.2015.08.004 doi: 10.1016/j.ocemod.2015.08.004

Pedlosky, J. (1987). Geophysical Fluid Dynamics. *New York and Berlin, Springer-Verlag, 1982. 636 ...*, 742. doi: 10.1007/978-1-4612-4650-3

Rintoul, S. R. (2018). The global influence of localized dynamics in the southern ocean. *Nature*, *558*(7709), 209–218.

Sallee, J.-B., Speer, K., & Rintoul, S. (2011). Mean-flow and topographic control on surface eddy-mixing in the southern ocean. *Journal of Marine Research*, *69*(4-5), 753–777.

Talley, L. D. (2013). Closure of the global overturning circulation through the indian, pacific, and southern oceans: Schematics and transports. *Oceanography*, *26*(1), 80–97.

Tamsitt, V., Abernathey, R. P., Mazloff, M. R., Wang, J., & Talley, L. D. (2018, mar). Transformation of Deep Water Masses Along Lagrangian Upwelling Pathways in the Southern Ocean. *Journal of Geophysical Research: Oceans*, *123*(3), 1994–2017. Retrieved from http://doi.wiley.com/10.1002/2017JC013409 doi: 10.1002/2017JC013409

Thompson, A. F., & Naveira Garabato, A. C. (2014). Equilibration of the Antarctic Circumpolar Current by Standing Meanders. *Journal of Physical Oceanography*, *44*(7), 1811–1828. doi: 10.1175/JPO-D-13-0163.1

Viebahn, J., & Eden, C. (2012). Standing eddies in the meridional overturning circulation. *Journal of physical oceanography*, *42*(9), 1486–1508.

Viglione, G. A., & Thompson, A. F. (2016, aug). Lagrangian pathways of upwelling in the Southern Ocean. *Journal of Geophysical Research: Oceans*, *121*(8), 6295–6309. Retrieved from http://doi.wiley.com/10.1002/2016JC011773 doi: 10.1002/2016JC011773

Young, W. R. (2012). An exact thickness-weighted average formulation of the boussinesq equations. *Journal of Physical Oceanography*, *42*(5), 692–707.

Youngs, M. K. (2020). *Residual overturning circulation and its connection to southern ocean dynamics* (Unpublished doctoral dissertation). Massachusetts Institute of Technology.

Youngs, M. K., Flierl, G. R., & Ferrari, R. (2019, nov). Role of residual overturning for the sensitivity of southern ocean isopycnal slopes to changes in wind forcing. *Journal of Physical Oceanography*, *49*(11), 2867–2881. Retrieved from www.ametsoc.org/PUBSReuseLicenses doi: 10.1175/JPO-D-19-0072.1

Youngs, M. K., Thompson, A. F., Lazar, A., & Richards, K. J. (2017). ACC Meanders, Energy Transfer, and Mixed Barotropic-Baroclinic Instability. *Journal of Physical Oceanography*, *47*(6), 1291–1305. doi: 10.1175/JPO-D-16-0160.1

Zhai, X., & Munday, D. R. (2014). Sensitivity of Southern Ocean overturning to wind stress changes: Role of surface restoring time scales. *Ocean Modelling*, *84*, 12–25. Retrieved from https://ac.els-cdn.com/S1463500314001358/1-s2.0-S1463500314001358-main.pdf?{_}tid=5dea6b1a-7a34-4552-a66b-4f38cc5fac79{\&}acdnat=1525449690{_}f83aba3ebee77f549d718fe26c4a0547 doi: 10.1016/j.ocemod.2014.09.004